Catalytic Self-Limited Assembly at Hard Templates: A Mesoscale Approach to Graphene Nanoshells for Lithium–Sulfur Batteries

Hong-Jie Peng,[†,⊥] Jiyuan Liang,[‡,⊥] Lin Zhu,[†,§,⊥] Jia-Qi Huang,[†] Xin-Bing Cheng,[†] Xuefeng Guo,[*,‡] Weiping Ding,[‡] Wancheng Zhu,[*,§] and Qiang Zhang[*,†]

[†]Beijing Key Laboratory of Green Chemical Reaction Engineering and Technology, Department of Chemical Engineering, Tsinghua University, Beijing 100084, China, [‡]Key Laboratory of Mesoscopic Chemistry, School of Chemistry and Chemical Engineering, Nanjing University, Nanjing 210093, China, and [§]Department of Chemical Engineering, Qufu Normal University, Qufu, Shandong 273165, China. [⊥]H.-J. Peng., J.-Y. Liang, and L. Zhu contributed equally to this work.

ABSTRACT Hollow nanostructures afford intriguing structural features ranging from large surface area and fully exposed active sites to kinetically favorable mass transportation and tunable surface permeability. The unique properties and potential applications of graphene nanoshells with well-defined small cavities and delicately designed graphene shells are strongly considered. Herein, a mesoscale approach to fabricate graphene nanoshells with a single or few graphene layers and quite small diameters through a catalytic self-limited assembly of nanographene on *in situ* formed nanoparticles was proposed. The graphene nanoshells with a diameter of ca. 10–30 nm and a pore volume of 1.98 $cm^3\ g^{-1}$ were employed as hosts to accommodate the sulfur for high-rate lithium–sulfur batteries. A very high initial discharge capacity of 1520 mAh g^{-1}, corresponding to 91% sulfur utilization rate at 0.1 C, was achieved on a graphene nanoshell/sulfur composite with 62 wt % loading. A very high retention of 70% was maintained when the current density increased from 0.1 C to 2.0 C, and an ultraslow decay rate of 0.06% per cycle during 1000 cycles was detected.

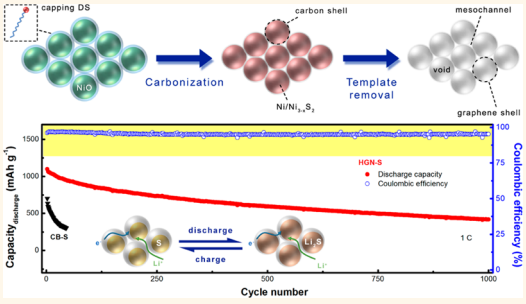

KEYWORDS: graphene · porous carbon · battery · nanostructures · sulfur

Hollow micro/nanostructures are of great interest for a myriad of applications such as catalysis, adsorption, chemical sensors, drug/gene delivery, and energy storage/conversion systems, which are endowed by their intriguing structural features ranging from large surface area and fully exposed active sites to kinetically favorable mass transportation and tunable surface permeability.[1] In particular, hollow nanocrystals integrating mesoscale hollow structure, nanoscale quantum effects, and atomic-scale periodic arrangement are gaining tremendous attention for both fundamental studies and practical applications.[2,3] Hollow graphene nanoshells (HGNs), which manifest not only the inherent structural benefits of hollow nanocrystals but also intrinsically extraordinary properties of nanographene units such as electrical conductivity, surface functionality, mechanical/chemical stability, and biocompatibility, are specifically fascinating for chemistry, material science, and biotechnology.[4,5] The unique properties and potential applications of hollow nanocrystals especially HGNs with well-defined cavities and delicately designed shells can be further explored if there are feasible routes for their efficient fabrication.

Great efforts have been dedicated to effectively synthesize hollow nanocrystals. The template-free or self-templating bottom-up approaches involving fantastic chemistry such as Kirkendall effects,[3,6] local Ostwald ripening,[7] and galvanic replacement[2,8] have demonstrated their feasibility and effectiveness to prepare high-quality metal/metal oxide/metal chalcogenide hollow nanocrystals. However, this unique

* Address correspondence to X.F.G. (guoxf@nju.edu.cn); W.C.Z. (zhuwancheng@tsinghua.org.cn); or Q.Z. (zhang-qiang@mails.tsinghua.edu.cn).

Received for review July 19, 2014 and accepted October 22, 2014.

Published online October 22, 2014
10.1021/nn503985s

physiochemical mechanism is limited to narrow synthetic diagrams and hardly extended to HGN synthesis. A template-involving top-down strategy is still the most versatile and effective methodology to fabricate hollow micro/nanostructures with a narrow size distribution, especially hollow carbon nanoshells. However, the atomic-/nano/microstructures of hollow carbon nanoshells are directly determined by specific templates, while the most commonly employed hard/soft templates including colloidal particles,[9] organic−organic assemblies,[10] and monodisperse multiphase systems[11,12] are always microsized and manifest no catalytic capability to regularly manage the arrangement of carbon atoms. Thus, controllable synthesis of HGNs with an engineered hollow cavity, predetermined layer number, small size, and highly crystalline few-layer graphene shells is rarely achieved. The key issue is the mesoscale bottom-up assembly of hierarchical atomic carbon sources, nanoscale hollow crystals, and sophisticated micro/macrostructures.

Lithium−sulfur batteries are nowadays undergoing a tremendous number of investigations due to the high theoretical energy density of 2600 Wh kg^{-1}. In addition, the cathode material sulfur is naturally abundant, economically effective, and environmentally friendly.[13−16] However, lithium−sulfur batteries are still suffer from poor cycling life and rate performance due to the intrinsic insulate sulfur/lithium sulfides and dissolution of intermediate polysulfide species for irreversible loss. Graphene[17−20] and other nanostructured carbon materials (*e.g.*, carbon nanotubes (CNTs),[21,22] porous carbon,[23−27] and their hybrids[28,29]) have been demonstrated to be advanced host materials for sulfur cathodes to circumvent the aforementioned issues. However, integrating all the structural benefits such as high specific surface area (SSA), good conductivity, interconnected ion channels, confined nanospace, and mechanical stability to improve the utilization of active materials and immobilize migratory polysulfides has still not been fully demonstrated. The concept of HGNs might be a promising strategy, which yet calls for new synthetic methodology.

In general, graphene can be controllably deposited on metal/metal oxides.[20,30−33] The use of uniform nanoparticles (NPs) as hard templates as well as working catalysts is expected to be an efficient and effective way to obtain graphene nanospheres with well-defined size. These tiny templates can be facilely removed by etching for hollow graphene spheres with high purity. The use of nanosized metal based catalysts is a promising top-down route for HGN fabrication, but the pure metal nanoparticles without ligand protection are always preferred to sinter into large NPs at high temperatures if there is no graphene predeposited on the surface.

In this contribution, a mesoscale catalytic self-limited assembly of hollow graphene spheres was proposed. The *in situ* formed nickel-based NPs were explored as both hard templates and working catalysts for template deposition of graphene with anticipated nanostructures. The pre-existing dodecyl sulfate (DS) among the catalyst precursors serves as the carbon source for the self-limited assembly. The good combination of catalytic deposition and precise replication of graphene in a one-pot synthesis will shed new light on controllable synthesis of hollow nanocrystals with a tunable interior space, interconnected mesopores, highly crystallized shell material, and a self-assembled mesostructure. In our case, zero-dimensional (0D) HGNs construct two-dimensional (2D) nanosheets and then assemble into a three-dimensional (3D) mesostructure, which manifests high capacity with good cyclability and superior rate performance as a promising host material for sulfur composite cathodes in lithium−sulfur battery applications.

RESULTS AND DISCUSSION

The *in situ* catalytic self-limited assembly of HGNs is schematically illustrated in Figure 1. DS-intercalated α-$Ni(OH)_2$ (α-$Ni(OH)_2$-DS) precursors were first obtained by a modified precipitation approach and then dehydrated to form DS-capped nanosheets of NiO NPs. With temperature rising to 800 °C, the capping DSs were pyrolyzed into small carbon molecules or carbon segments, which dissolved in NiO phase and catalytically recombined on the surface of NP hard templates to form highly graphitic structures. The NiO NPs were simultaneously reduced or sulfurized into Ni/$Ni_{3-x}S_2$ NPs. The HGN nanostructure was eventually available by acid etching templates. Since the aggregation of NPs remains a major obstacle for their intriguing applications, the DS herein displays two major functionalities of (1) capping agents to efficiently preventing the α-$Ni(OH)_2$ layers/NiO NPs from stacking/aggregating and (2) serving as a carbon source by carbonizing long-chain dodecyl and realizing the self-limited assembly of single-/few-layer graphene shells. Furthermore, such a facile and versatile method also affords wide potential for various hollow nanocrystals by mediating the host−guest chemistry between precursor molecule guests and catalytic NP hosts, the topological structure of precursors, and local chemical circumstance.

As scanning electron microscopy (SEM) and transmission electron microscopy (TEM) images indicated, the α-$Ni(OH)_2$-DS precursor exhibits a flower-like morphology assembled by layered α-$Ni(OH)_2$ nanosheets with a thickness of 30−50 nm and high curvature (Figure 2a). This is mainly attributed to the assistance and intercalation of DS anions during precipitation. The interlayer DS anions are confirmed by the appearance of bands at 2920 and 2851 cm^{-1} in the Fourier transform infrared (FTIR) spectrum of α-$Ni(OH)_2$-DS compared to pristine α-$Ni(OH)_2$, which is ascribed to

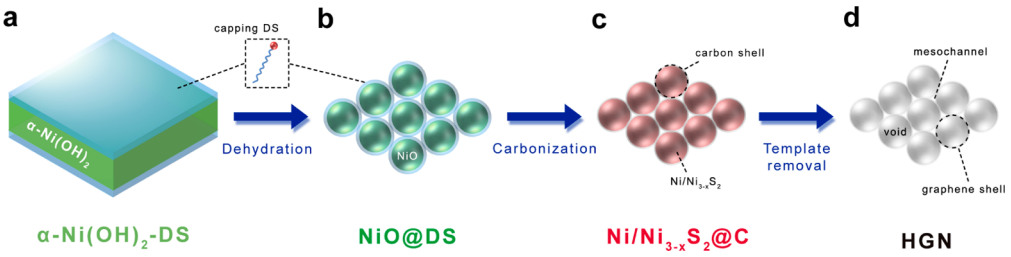

Figure 1. Schematic illustration of the *in situ* catalytic self-limited assembly of HGNs. A facile bifunctional template strategy to fabricate HGNs with nanosized hollow voids and few-layer graphene shells: (a) modified precipitation of α-Ni(OH)$_2$-DS; (b) *in situ* calcination toward NiO@DS; (c) carbonization into Ni/Ni$_{3-x}$S$_2$@C; (d) HGNs after template removal.

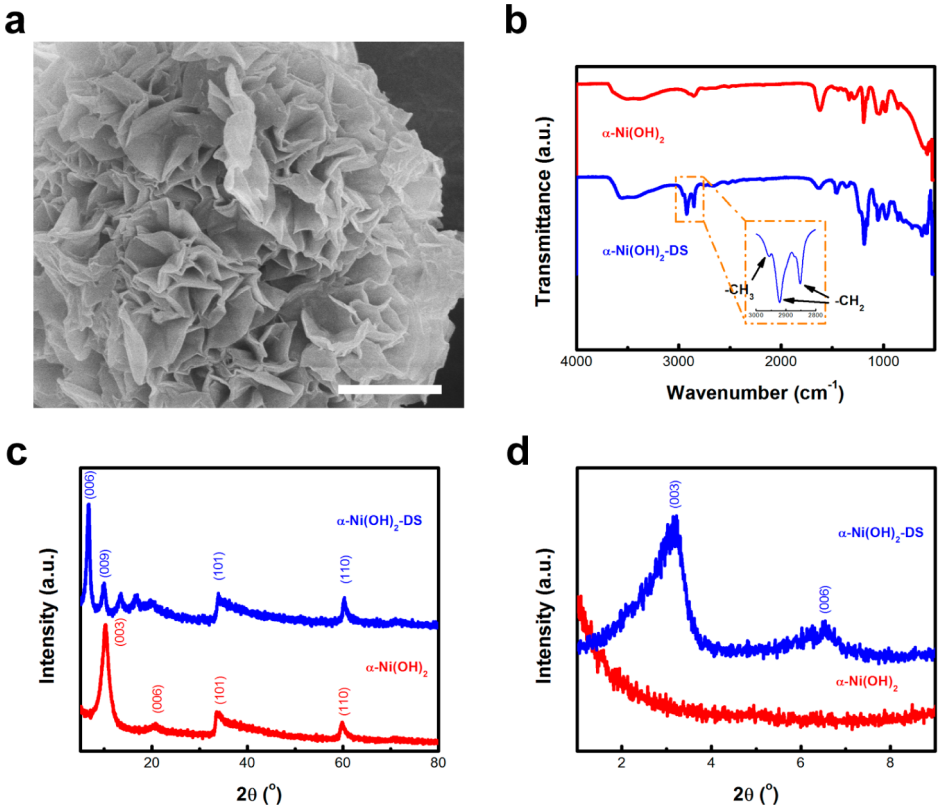

Figure 2. Morphology and structure of α-Ni(OH)$_2$-DS precursors. (a) SEM image, (b) FTIR spectra, (c, d) XRD patterns. The scale bar in part a is 1 μm.

the asymmetric and symmetric $-CH_2$ stretching vibrations of alkyl chains of DS, respectively (Figure 2b), while the relatively weak band at 2954 cm^{-1} corresponds to a stretching vibration of the terminal $-CH_3$ group of the hydrocarbon tail. A distinct reflection in the low-angle region ($2\theta < 25°$) of X-ray diffraction (XRD) patterns indicates the regular arrangement of (00*l*) planes and the layered structure of α-Ni(OH)$_2$ (Figure 2c). With the introduction of DS chains into the α-Ni(OH)$_2$ interlayer, a series of Basal peaks remarkably shifts to lower angles, suggesting that the long-chain DSs intercalate into the interlayer galleries, while the turbostratic 2D α-Ni(OH)$_2$ laminates indicated by the asymmetric nature of (101) and (110) planes are still well preserved (Figure 2c,d). As a result, the *d*-spacing of the (003) and (006) planes along the *c*-axis increases from 0.86 nm to 2.76 nm and 0.43 nm to 0.66 nm, respectively, the multiple reflection of which indicates the different topological status of intercalated DS anions.

The Ni/Ni$_{3-x}$S$_2$@C nanosheets were assembled by uniformly distributed NPs *via* a facile one-step pyrolysis of α-Ni(OH)$_2$-DS precursors. The NPs range from several to several hundred nanometers (Figure 3a). The formation of larger particles with a size of 100−400 nm is mainly induced by an inevitable Ostwald ripening effect of NPs at temperatures as high as 800 °C. However, most of the NPs are prevented from sintering due to the capping DS anions for the efficient deposition of graphene (Figure 3b). These NPs are encapsulated in a thin carbon wall and embedded in thin nanoflakes. The carbon walls are mainly composed of few-layer graphene shells as the adjacent graphitic (002) plane of 0.34 nm indicated, while the individual

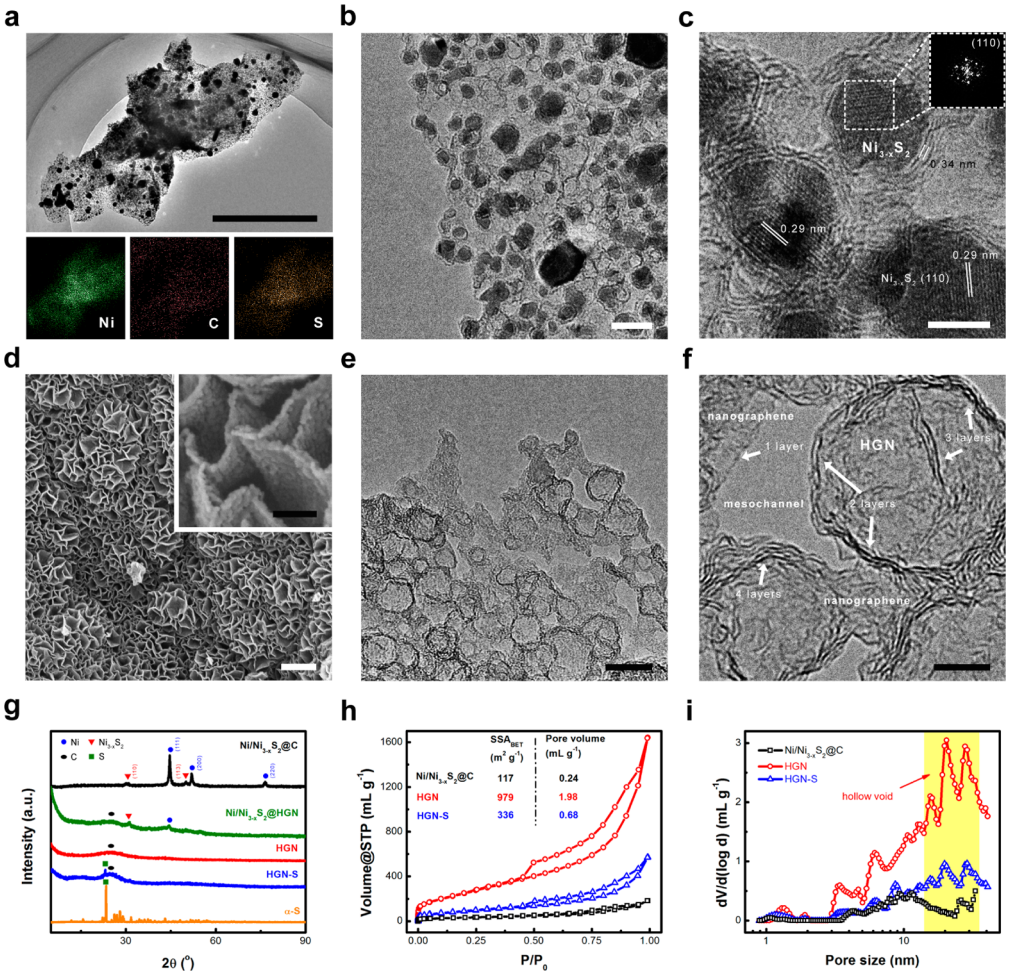

Figure 3. Morphology and structure of HGNs. (a, b) TEM and corresponding energy dispersive spectroscopy (EDS) mapping of elemental Ni, C, and S (inset of a) and (c) high-resolution (HR-TEM) images of $Ni/Ni_{3-x}S_2$@C. The scale bars in a, b, and c are 1 μm, 20 nm, and 5 nm, respectively. (d) SEM, high magnification of SEM (inset of d), (e) TEM, and (f) HR-TEM images of HGNs. The scale bars in d, inset of d, e, and f are 1 μm, 100 nm, 20 nm, and 5 nm, respectively. (g) XRD patterns of $Ni/Ni_{3-x}S_2$@C, $Ni/Ni_{3-x}S_2$@C with partially removed NPs (denoted as $Ni/Ni_{3-x}S_2$@HGN), HGN, and HGN-S. (h) N_2 adsorption isotherms, corresponding BET specific surface area, pore volume, and (i) pore-size distribution of $Ni/Ni_{3-x}S_2$@C, HGN, and HGN-S.

NP is a single crystal of heazlewoodite $Ni_{3-x}S_2$ as the quasi-hexagonal patterns of the fast Fourier transform (FFT) image and the (110) plane with a *d*-spacing of 0.29 nm suggested simultaneously (Figure 3c). A 3D flower-like mesostructure can be formed by removing the templates. The flower-like nanoarchitecture is assembled by highly curved thin flakes with a thickness of *ca.* 20−30 nm, while 2D nanosheets are composed of a single layer of 0D HGNs since most of the HGNs have a diameter of 20−30 nm (Figure 3d). No crack or hole can be observed on the outer shell of the HGNs. HGNs inherit the hierarchical structure of precursors due to the *in situ* hard-template replication. The size of the hollow interior is mostly around 10−30 nm (Figure S1), the outer shell is of few-layer nanographene attached with some amorphous carbon, and interconnected mesochannels are also well constructed (Figure 3e,f). Abundant defects and edges on the outer graphene shells are not only observed in the high-resolution TEM image but also indicated by Raman spectra, which will be beneficial for ion transfer in electrochemical applications and mass release in biomedical usage (Figure S2). A strong sp^2-hybridized carbon attributed to the graphene can be detected by the X-ray photoelectron spectroscopy (XPS) analysis (Figure S3). Despite the high density of surface defects, the conductivity of HGN reaches 695 S m^{-1}, which is comparable to highly crystallized CNTs.[34]

Phase evolution during the replication of the HGN nanostructure is elaborated by XRD patterns (Figure 3g). Both the Ni and $Ni_{3-x}S_2$ phase with good crystallization can be observed in pyrolysis products, which are derived from reduction and sulfuration of NiO by hydrocarbons and sulfates in capping DSs, respectively. By gradually removing the NP templates, the reflections of $Ni/Ni_{3-x}S_2$ further weaken and disappear, while the emerging band at around 26° indicates the graphitic domain of hollow crystalline shells. The N_2 isothermal adsorption indicates the mesoporous structure of $Ni/Ni_{3-x}S_2$@C with a relatively

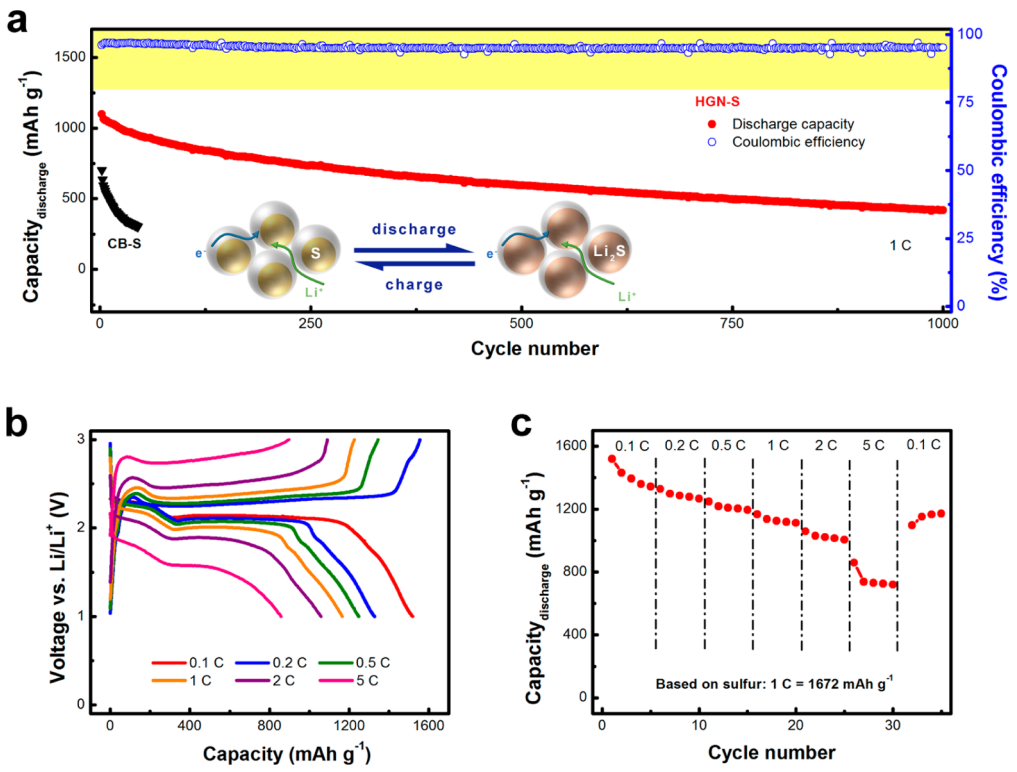

Figure 4. Electrochemical performance of HGN-S. (a) Cycling performance at current density of 1 C and schematic illustration of HGN-S during discharge and charge (inset), (b) galvanostatic charge−discharge profiles at different current densities, and (c) rate performance.

broad pore size distribution of 4−20 nm, which is attributed to the interspacing of NPs (Figure 3h,i). The removal of NP templates renders as-obtained HGNs with a great increase in both Brunauer−Emmett−Teller (BET) SSA to 979 $m^2\ g^{-1}$ and pore volume to 1.98 mL g^{-1}. Meanwhile, the great increase in pore volume at the pore size range 10−30 nm can also be assigned to the interior voids that used to be occupied by NP templates. Thus, the rationally engineered HGN nanostructure possesses outstanding advantages such as (1) a unique nanosized hollow interior to accommodate active materials and volume expansion, (2) interconnected few-layer graphene with good electrical contact and transfer properties, and (3) short diffusion length along the thin 2D nanosheets and 3D nanoflower mesoarchitecture for rapid ion transport, which is of paramount importance in promising electrode materials in advanced energy storage systems.

To implement our proof-of-concept, HGNs are employed as host materials for sulfur composite cathodes in lithium−sulfur batteries. The sulfur is infiltrated in HGNs *via* a facile melt−diffuse method to obtain an HGN-S composite with 62 wt % content of sulfur (Figure S4a). The 3D flower-like morphology of HGNs is well preserved with no bulky sulfur particles observed (Figure S4b). Due to the high SSA of HGNs and their affinity to sulfur, sulfur is favorably distributed in the carbon nanosheets (Figure S4c). The strong confinement in the hollow interior of HGNs of sulfur is further demonstrated by weakened signals of XRD patterns and the Raman spectrum (Figures 3g and S5). The hierarchical porous structure of carbon hosts is partially occupied by sulfur guests, resulting in a decrease of the SSA to 336 $m^2\ g^{-1}$ and pore volume to 0.68 $cm^3\ g^{-1}$ (Figure 3h,i). Sulfur is tightly attached on the hollow graphene shells (Figure S4d). However, there are sufficient space and ion channels to accommodate greatly expanded discharge products of lithium sulfides and intermediate polysulfides as well as electrolytes, which is favorable for high sulfur utilization and robust cycling.

The electrochemical properties of the HGN-S composite cathode are evaluated in coin cells. Two-step reduction of elemental sulfur into high-order polysulfides and subsequent lithium sulfides as well as its counterpart oxidation are illustrated by cyclic voltammetry (CV) profiles, indicating the stable and reversible redox reactions (Figure S6a). With a current density of 1.0 C (1.0 C = 1675 mA g^{-1}), a high initial discharge capacity of 1098 mAh g^{-1} is achieved, corresponding to 66% utilization of sulfur (Figure 4a). After 1000 cycles, the capacity gradually decreased to 419 mAh g^{-1} with an average decay rate of 0.06% per cycle, combined with a stabilized Coulombic efficiency as high as 95% with no lithium nitrate addition. Cycling performance at different current rates manifests similar capacity retention (Figure S7). Both stability and efficiency are significantly better than other reported

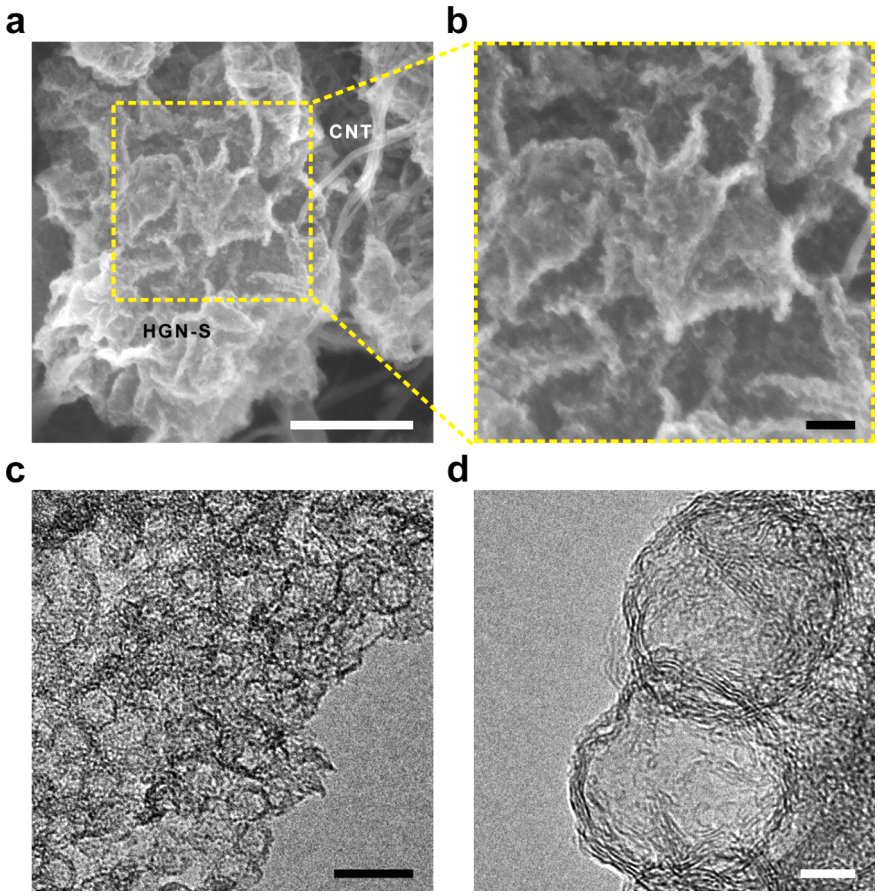

Figure 5. Morphology of cycled HGN-S electrodes: (a) SEM, (b) high-resolution SEM of selected area in (a), (c) TEM, and (d) high-magnification TEM images of HGN-S electrodes after 1000 cycles.

graphene-based sulfur cathodes.[18−20] This superiority is ascribed to (1) the unique nanosized hollow interior to relieve structural stress during volume expansion/contraction and (2) nanoscale confined active material with good electron/ion accessibility for long-term cycling. In contrast, carbon black (CB) as solid spheres with similar size and amorphous carbon texture is employed for comparison, unsurprisingly exhibiting much lower capacity and stability (Figure 4a). The further promotion of stability and efficiency can be demonstrated by applying effective electrolyte or separator systems.[25,35−37] Besides, recent advances in chemically doped carbon for lithium−sulfur batteries also provide another direction to stabilize the carbon/sulfur interfaces and result in better performance.[27,34] More importantly, due to the dominant advantage on mass transportation afforded by an interconnected hollow structure, outstanding rate performance of 1520, 1058, and 859 mAh g^{-1} at current densities of 0.1, 2.0, and 5.0 C is manifested, respectively (Figure 4b,c). Even at a high rate of 5.0 C (8.4 A g^{-1}), the two-step galvanostatic discharge profiles are still maintained while the decrease of utilization at high rate is mainly attributed to the blockage by deep lithiation to lithium sulfides, as this process is kinetically inert. This favorable high rate performance is supported by low charge-transfer resistance, as electrochemical impedance spectroscopy (EIS) indicated (Figure S6b). Even considering the mass of conductive agents and the binder, the capacities based on the whole electrode are still comparable to state-of-the-art lithium−sulfur batteries. Yet the high performance with a high-areal sulfur loading amount should be further exploited to improve the energy density of the whole cell (Table S1).

The structural stability is also crucial for stable cycling. Even after 1000 cycles, HGN-S in the cycled electrodes still manifests a flower-like mesostructure assembled by 2D carbon nanosheets, in which hollow graphene nanoshells are sustained compactly (Figure 5a,b). TEM images indicate that no obvious crack can be observed and the graphene nanoshells still possess both an intact hollow void and few-layer graphene walls (Figure 5c,d). It can be inferred that reserved interior space can not only sequester soluble species but also accommodate a huge volume fluctuation, which synergistically contribute to a stable electrochemical performance.

The mesoscale catalytic self-limited assembly is quite efficient and effective for HGN formation, which was attributed to (1) the *in situ* generated nickel-containing hard templates having good contact with

carbon sources; compared with the routine top-down method with silica and polymer colloid templates, the DS carbon precursors were premixed with the nickel-containing hard templates *at an atomic scale* through a facile host–guest chemistry, which guarantees the supply of carbon sources and simultaneously realizes the self-limited replication of single-/few-layer graphene; (2) the *in situ* generated nickel-containing hard templates also served as catalysts for self-assembly of carbon atoms into graphene with high efficiency due to the favorable affinity of nickel to carbon seeds; (3) most of the *in situ* generated templates had a uniform size at a scale of *ca.* 20 nm, which is much smaller than the routine colloid templates for hollow sphere formation, with a size of 50–1000 nm; (4) the catalytic formation of graphene can also be expected to be available on other transitional metal-containing NPs (*e.g.*, cobalt, iron, copper) according to the recent advances in the general rules of chemical deposition of graphene on metal-containing NPs;[32] (5) the hard templates reported herein can be easily removed through facile acid leaching, and HGNs with a purity of over 99% were available (Figure S8).

The nanostructured carbon materials are efficient and effective candidates to improve the sulfur utilization and restrain the polysulfide shuttle for lithium–sulfur batteries.[15,16] The use of hollow spheres also takes advantage of higher sulfur content while still retaining the benefits of a porous carbon that inhibits polysulfide dissolution.[38] For instance, microporous carbon spheres with a diameter of 200–300 nm and a specific surface area of 843.5 $m^2 g^{-1}$ were employed to entrap 42 wt % sulfur, which delivered a high initial discharge capacity of 1180 mAh g^{-1} at a current density of 400 mA g^{-1}.[39] Archer and co-workers found the porous hollow carbon spheres with a diameter of 300–350 nm and a pore volume of 0.82 g cm^{-3} can accommodate 70% sulfur, which renders an initial discharge rate of 1071 mAh g^{-1} at a rate of 0.5 C.[40] Other spheres, such as double-shelled hollow carbon spheres,[41] porous hollow carbon spheres,[38,42–44] porous graphitic carbon,[45] hierarchically micro/mesoporous carbon spheres,[23,25] soft-templated carbonaceous nanospheres,[46] polymer (polyvinylpyrrolidone)-encapsulated hollow sulfur nanospheres,[47] and sulfur–TiO_2 yolk–shell nanoarchitectures[48] with a size of 150–500 nm were also explored as a host for sulfur. Peapod-like mesoporous carbon was synthesized and used as the matrix to fabricate a carbon/sulfur composite.[49] These obtained composites have demonstrated outstanding features for lithium–sulfur batteries, and the sulfur utilization ratio can be further improved if small spheres are employed. Recently, 500–2000 nm, durable carbon-coated Li_2S core–shell spheres with a high initial discharge capacity of 972 mAh g^{-1} Li_2S (1394 mAh g^{-1} S) at the 0.2 C rate were also proposed.[50] Herein, the HGNs with an average size of 20 nm are good scaffolds to entrap and sequester sulfur in their interiors for lithium–sulfur batteries. Compared with CNTs,[21,22] graphene,[17–20] porous carbon,[24,26] or their hybrids[28,29] as frameworks with open structures, this use of HGNs offers (1) a large amount of small-size sulfur sequestered by the capsules, which guarantees a high utilization of 91% (corresponding to 1520 mAh g^{-1}) at 0.1 C, (2) free space for sulfur expansion during discharge even with a high sulfur loading of 62%, (3) slowing of the dissolution of lithium polysulfide and parasitic shuttle *via* close spherical space, (4) excellent electron pathways among the insulate sulfur/Li_2S_2/Li_2S, graphene, and conductive agent, and (5) intercrossed ion channels for rapid diffusion of ions, which affords 70% retention when the current rate increases from 0.1 C to 2.0 C. Therefore, the large amount of sulfur confined by small spheres with continuous 3D graphene frameworks can be utilized in high ratio, while the rate performance and cycling performance can be well maintained.

CONCLUSIONS

HGNs with a quite small diameter, single/few graphitic layers, and 3D hierarchical flower-like morphology were fabricated through a mesoscale catalytic self-limited assembly strategy. The *in situ* formed nickel-based NPs served as both hard templates and working catalysts for hard-template deposition of graphene with well-defined 3D nanostructures. The HGNs with a diameter of 10–30 nm, an SSA as high as 979 $m^2 g^{-1}$, and a pore volume of 1.98 $cm^3 g^{-1}$ were employed as host to accommodate sulfur for high-rate lithium–sulfur batteries. Such small graphene spheres offer outstanding advantages of good confinement of small sulfur particles, high surface area to entrap polysulfides, intercrossed ion channels, and interlinked electron pathways. Therefore, the HGN-S cathode delivered high discharge capacities of 1520, 1058, and 737 mAh g^{-1}, which were also achieved at different current densities of 0.1, 2.0, and 5.0 C, respectively. A high initial discharge capacity of 1098 mAh g^{-1} and a discharge capacity of 419 mAh g^{-1} were obtained after 1000 cycles at a current density of 1.0 C. The decay rate was 0.06% per cycle, which is significantly lower than the value of other lithium–sulfur batteries based on graphene in lithium nitrate free electrolytes. To the best of our knowledge, the HGNs reported herein are the first example of hollow nanocrystals to deliver an extended lifetime of 1000 cycles and high rate performance. The good combination of bottom-up strategy of metal-based NP catalyst formation and top-down route of graphene deposition in a one-pot synthesis will shed new light not only on controllable synthesis of hollow nanocrystals with a tunable interior space, interconnected mesopores, highly crystallized shell material, and a self-assembled mesostructure, but also

on their unique properties of graphene nanoshells with small sizes and their promising applications for lithium–sulfur batteries, supercapacitors, solar cells, nanocomposites, desalination, oil absorption, heavy metal removal, drug delivery, and controlled release.

EXPERIMENTAL SECTION

Synthesis of Precursor α-Ni(OH)$_2$-DS Powders. α-Ni(OH)$_2$-DSs were synthesized by a facile precipitation of an aqueous solution of nickel chloride and sodium dodecyl sulfate (SDS) through hexamethylenetetramine (HMT) hydrolysis. In a typical synthesis process, 0.10 M $NiCl_2 \cdot 6H_2O$, 0.30 M HMT, and 0.20 M SDS solution were mixed in a 100 mL three-neck bottle. The mixed solution was heated at 95 °C for 24.0 h under mild stirring. A suspension containing a green precipitate was isolated after the reaction, washed with distilled water to remove excess surfactant, and finally dried at room temperature.

Synthesis of HGNs. The α-Ni(OH)$_2$-DS powders were heated at a rate of 5 °C min^{-1} to 200 °C under an Ar atmosphere and kept at that temperature for 2.0 h, then to 800 °C for another 3.0 h. The sample with partially removed NPs was prepared by treating the carbonized product of 100 mg with 37 wt % HCl solution of 100 mL under room temperature for a relatively short period of 1.0 h. To obtain high-purity HGNs, the carbonized product of 100 mg was combined with a 37 wt % HCl solution of 100 mL under a high temperature of 70 °C for a long period of 12.0 h. The resulting HGNs were filtered, washed with distilled water, and dried at 80 °C. A 9.5 wt % carbon yield defined as the ratio of HGN weight and carbon precursor weight was obtained.

Fabrication of HGN-S Cathodes. The sulfur powder with a purity of >99.9% was purchased from Alfa Aesar without further purification. A coheating procedure was employed to accommodate the sulfur into the hollow space of the HGNs. Typically, sulfur powder was mixed with the HGNs with a mass ratio of 7:3 in an agate mortar and strongly ground for 10 min. The as-obtained HGN-S mixtures were heated to 155 °C in a sealed quartz bottle. With a 4.0 h heating, the sulfur successfully immersed into the inner space of the spheres under vacuum and HGN-S composite cathodes were obtained.

Electrochemical Evaluation. To assemble a lithium–sulfur cell with an HGN-S cathode, the electrode was constructed with HGN-S composites, CNT conductive additives, and poly(vinylidene fluoride) (PVDF) binder in *N*-methyl-2-pyrrolidone at a mass ratio of HGN-S:CNT:PVDF = 85:10:5. The slurry was homogeneously mixed by a magnetic stirrer for ca. 24.0 h. Doctor blade coating was employed to coat the slurry onto a 20 μm aluminum current collector, and a vacuum drying at 60 °C was subsequently carried out for 6.0 h. An areal loading of 1.1 mg cm^{-2} was obtained. Disks of 13 mm were punched as the working cathodes for the lithium–sulfur cells. The CB-S cathode as a comparison was fabricated by only changing the carbon/sulfur composite from HGN-S to CB-S, which was prepared by mixing and heating SuperP and sulfur at the same condition.

Standard 2025 coin-type cells with two-electrode cell configuration were employed. Dimethyl ether and 1,3-dioxolane with a volume ratio of 1:1 dissolved in 1.0 mol L^{-1} lithium bis(trifluoromethanesulfonyl)imide was selected as electrolyte, 1.0 mm thick Li metal foil was used as the anode, and Celgard 2400 polypropylene membranes acted as the separator. The lithium–sulfur cells were assembled in an argon-filled glovebox. Both the CV and EIS measurements were performed on a Solartron 1470E electrochemical workstation. CV measurements were performed at a scan rate of 0.1 mV s^{-1}. EIS measurements were conducted in the frequency range of 10^{-2}–10^5 Hz. The cyclic performance was collected with a Neware multichannel battery cycler with a voltage window of 1.8–2.8 V.

Structure Characterizations. The structure of the electrodes of interest was identified by an X-ray powder diffractometer (XRD, D8-Advance, Bruker, Germany). The morphology of HGNs and HGN-S composites were characterized by a transmission electron microscope (JEM 2010, JEOL Ltd., Tokyo, Japan) at 120.0 kV and a field scanning electron microscope (JSM 7401F, JEOL Ltd., Tokyo, Japan) at 3.0 kV. The Raman spectra of the HGNs and HGN-S cathode were recorded using a Horiba Jobin Yvon LabRAM HR800 Raman spectrometer with He–Ne laser excitation at 633 nm. The sulfur ratio in the HGN-S composites was determined by thermogravimetry analysis (TGA) using a TGA/DSC1 STAR^e system in a N_2 atmosphere with a temperature ramp rate of 20 °C min^{-1}. An Autosorb-IQ2-MP-C adsorption analyzer was employed to record the N_2 adsorption–desorption isotherms of the HGN-S composites at −196 °C. Before N_2 sorption isotherm measurements, the sample was degassed at a very low temperature of 50 °C until a manifold pressure of 2.0 mmHg was achieved to avoid sulfur sublimation. The surface area was determined by the BET method in the P/P_0 range 0.05–0.30, and the pore size distribution plot was calculated by the quenched solid density functional theory using the adsorption branch. The pore geometry was determined as having a slit pore of <2 nm, a cylindrical pore of 2–5 nm, and a spherical pore of >5 nm. The FT-IR spectrum was collected using a Nicolet 6700 spectrometer. The four-probe method was performed to determine the powder conductivity of the HGNs, which were compressed into a dense disk with a diameter of 13.0 mm under a pressure of 8.0 MPa.

Conflict of Interest: The authors declare no competing financial interest.

Supporting Information Available: TEM image of the α-Ni(OH)$_2$-DS precursor, Raman spectra of HGNs and HGN-S composites, and the electrochemical behaviors are available free of charge via the Internet at http://pubs.acs.org.

Acknowledgment. This work was supported by the Natural Scientific Foundation of China (Nos. 21306103, 21276141, 21273109, 21173119).

REFERENCES AND NOTES

1. Lou, X. W.; Archer, L. A.; Yang, Z. C. Hollow Micro-/Nanostructures: Synthesis and Applications. *Adv. Mater.* **2008**, *20*, 3987–4019.
2. Sun, Y. G.; Xia, Y. N. Shape-Controlled Synthesis of Gold and Silver Nanoparticles. *Science* **2002**, *298*, 2176–2179.
3. Yin, Y. D.; Rioux, R. M.; Erdonmez, C. K.; Hughes, S.; Somorjai, G. A.; Alivisatos, A. P. Formation of Hollow Nanocrystals through the Nanoscale Kirkendall Effect. *Science* **2004**, *304*, 711–714.
4. Nardecchia, S.; Carriazo, D.; Ferrer, M. L.; Gutierrez, M. C.; del Monte, F. Three Dimensional Macroporous Architectures and Aerogels Built of Carbon Nanotubes and/or Graphene: Synthesis and Applications. *Chem. Soc. Rev.* **2013**, *42*, 794–830.
5. Jiang, L. L.; Fan, Z. J. Design of Advanced Porous Graphene Materials: From Graphene Nanomesh to 3D Architectures. *Nanoscale* **2014**, *6*, 1922–1945.
6. Fan, H. J.; Knez, M.; Scholz, R.; Nielsch, K.; Pippel, E.; Hesse, D.; Zacharias, M.; Gosele, U. Monocrystalline Spinel Nanotube Fabrication Based on the Kirkendall Effect. *Nat. Mater.* **2006**, *5*, 627–631.
7. Lou, X. W.; Wang, Y.; Yuan, C. L.; Lee, J. Y.; Archer, L. A. Template-Free Synthesis of SnO_2 Hollow Nanostructures with High Lithium Storage Capacity. *Adv. Mater.* **2006**, *18*, 2325–2329.
8. Oh, M. H.; Yu, T.; Yu, S. H.; Lim, B.; Ko, K. T.; Willinger, M. G.; Seo, D. H.; Kim, B. H.; Cho, M. G.; Park, J. H.; *et al.* Galvanic Replacement Reactions in Metal Oxide Nanocrystals. *Science* **2013**, *340*, 964–968.
9. Wang, C. W.; Wang, Y.; Graser, J.; Zhao, R.; Gao, F.; O'Connell, M. J. Solution-Based Carbohydrate Synthesis

of Individual Solid, Hollow, and Porous Carbon Nanospheres Using Spray Pyrolysis. *ACS Nano* **2013**, *7*, 11156–11165.
10. Zhang, K.; Zhao, Q.; Tao, Z. L.; Chen, J. Composite of Sulfur Impregnated in Porous Hollow Carbon Spheres as the Cathode of Li-S Batteries with High Performance. *Nano Res.* **2013**, *6*, 38–46.
11. Choi, B. G.; Yang, M.; Hong, W. H.; Choi, J. W.; Huh, Y. S. 3D Macroporous Graphene Frameworks for Supercapacitors with High Energy and Power Densities. *ACS Nano* **2012**, *6*, 4020–4028.
12. Chen, C. M.; Zhang, Q.; Huang, C. H.; Zhao, X. C.; Zhang, B. S.; Kong, Q. Q.; Wang, M. Z.; Yang, Y. G.; Cai, R.; Su, D. S. Macroporous 'Bubble' Graphene Film *via* Template-Directed Ordered-Assembly for High Rate Supercapacitors. *Chem. Commun.* **2012**, *48*, 7149–7151.
13. Evers, S.; Nazar, L. F. New Approaches for High Energy Density Lithium-Sulfur Battery Cathodes. *Acc. Chem. Res.* **2013**, *46*, 1135–1143.
14. Manthiram, A.; Fu, Y.; Su, Y.-S. Challenges and Prospects of Lithium–Sulfur Batteries. *Acc. Chem. Res.* **2012**, *46*, 1125–1134.
15. Manthiram, A.; Fu, Y.; Chung, S.-H.; Zu, C.; Su, Y.-S. Rechargeable Lithium–Sulfur Batteries. *Chem. Rev.* **2014**, 10.1021/cr500062v.
16. Yang, Y.; Zheng, G.; Cui, Y. Nanostructured Sulfur Cathodes. *Chem. Soc. Rev.* **2013**, *42*, 3018–3032.
17. Zhou, G.; Yin, L.-C.; Wang, D.-W.; Li, L.; Pei, S.; Gentle, I. R.; Li, F.; Cheng, H.-M. Fibrous Hybrid of Graphene and Sulfur Nanocrystals for High-Performance Lithium–Sulfur Batteries. *ACS Nano* **2013**, *7*, 5367–5375.
18. Huang, J. Q.; Liu, X. F.; Zhang, Q.; Chen, C. M.; Zhao, M. Q.; Zhang, S. M.; Zhu, W. C.; Qian, W. Z.; Wei, F. Entrapment of Sulfur in Hierarchical Porous Graphene for Lithium-Sulfur Batteries with High Rate Performance from −40 to 60 °C. *Nano Energy* **2013**, *2*, 314–321.
19. Wang, H.; Yang, Y.; Liang, Y.; Robinson, J. T.; Li, Y.; Jackson, A.; Cui, Y.; Dai, H. Graphene-Wrapped Sulfur Particles as a Rechargeable Lithium–Sulfur Battery Cathode Material with High Capacity and Cycling Stability. *Nano Lett.* **2011**, *11*, 2644–2647.
20. Zhao, M.-Q.; Zhang, Q.; Huang, J.-Q.; Tian, G.-L.; Nie, J.-Q.; Peng, H.-J.; Wei, F. Unstacked Double-Layer Templated Graphene for High-Rate Lithium–Sulphur Batteries. *Nat. Commun.* **2014**, *5*, 3410.
21. Cheng, X.-B.; Huang, J.-Q.; Zhang, Q.; Peng, H.-J.; Zhao, M.-Q.; Wei, F. Aligned Carbon Nanotube/Sulfur Composite Cathodes with High Sulfur Content for Lithium-Sulfur Batteries. *Nano Energy* **2014**, *4*, 65–72.
22. Wang, L.; Dong, Z. H.; Wang, D.; Zhang, F. X.; Jin, J. Covalent Bond Glued Sulfur Nanosheet-Based Cathode Integration for Long-Cycle-Life Li-S Batteries. *Nano Lett.* **2013**, *13*, 6244–6250.
23. Li, Z.; Jiang, Y.; Yuan, L.; Yi, Z.; Wu, C.; Liu, Y.; Strasser, P.; Huang, Y. A Highly Ordered Meso@Micro-Porous Carbon Supported Sulfur@Smaller-Sulfur Core-Shell Structured Cathode for Li-S Batteries. *ACS Nano* **2014**, *8*, 9295–9303.
24. Oschatz, M.; Borchardt, L.; Pinkert, K.; Thieme, S.; Lohe, M. R.; Hoffmann, C.; Benusch, M.; Wisser, F. M.; Ziegler, C.; Giebeler, L.; *et al*. Hierarchical Carbide-Derived Carbon Foams with Advanced Mesostructure as a Versatile Electrochemical Energy-Storage Material. *Adv. Energy Mater.* **2014**, *4*, 1300645.
25. Lee, J. T.; Zhao, Y.; Thieme, S.; Kim, H.; Oschatz, M.; Borchardt, L.; Magasinski, A.; Cho, W.-I.; Kaskel, S.; Yushin, G. Sulfur-Infiltrated Micro- and Mesoporous Silicon Carbide-Derived Carbon Cathode for High-Performance Lithium Sulfur Batteries. *Adv. Mater.* **2013**, *25*, 4573–4579.
26. Ji, X. L.; Lee, K. T.; Nazar, L. F. A Highly Ordered Nanostructured Carbon-Sulphur Cathode for Lithium-Sulphur Batteries. *Nat. Mater.* **2009**, *8*, 500–506.
27. Song, J.; Xu, T.; Gordin, M. L.; Zhu, P.; Lv, D.; Jiang, Y.-B.; Chen, Y.; Duan, Y.; Wang, D. Nitrogen-Doped Mesoporous Carbon Promoted Chemical Adsorption of Sulfur and Fabrication of High-Areal-Capacity Sulfur Cathode with Exceptional Cycling Stability for Lithium-Sulfur Batteries. *Adv. Funct. Mater.* **2014**, *24*, 1243–1250.
28. Yang, X.; Zhang, L.; Zhang, F.; Huang, Y.; Chen, Y. Sulfur-Infiltrated Graphene-Based Layered Porous Carbon Cathodes for High-Performance Lithium–Sulfur Batteries. *ACS Nano* **2014**, *8*, 5208–5215.
29. Peng, H.-J.; Huang, J.-Q.; Zhao, M.-Q.; Zhang, Q.; Cheng, X.-B.; Liu, X.-Y.; Qian, W.-Z.; Wei, F. Nanoarchitectured Graphene/CNT@Porous Carbon with Extraordinary Electrical Conductivity and Interconnected Micro/Mesopores for Lithium-Sulfur Batteries. *Adv. Funct. Mater.* **2014**, *24*, 2772–2781.
30. Li, X. S.; Cai, W. W.; An, J. H.; Kim, S.; Nah, J.; Yang, D. X.; Piner, R.; Velamakanni, A.; Jung, I.; Tutuc, E.; *et al*. Large-Area Synthesis of High-Quality and Uniform Graphene Films on Copper Foils. *Science* **2009**, *324*, 1312–1314.
31. Chen, Z. P.; Ren, W. C.; Gao, L. B.; Liu, B. L.; Pei, S. F.; Cheng, H. M. Three-Dimensional Flexible and Conductive Interconnected Graphene Networks Grown by Chemical Vapour Deposition. *Nat. Mater.* **2011**, *10*, 424–428.
32. Yan, K.; Fu, L.; Peng, H. L.; Liu, Z. F. Designed CVD Growth of Graphene via Process Engineering. *Acc. Chem. Res.* **2013**, *46*, 2263–2274.
33. Hwang, J.; Kim, M.; Campbell, D.; Alsalman, H. A.; Kwak, J. Y.; Shivaraman, S.; Woll, A. R.; Singh, A. K.; Hennig, R. G.; Gorantla, S.; *et al*. van der Waals Epitaxial Growth of Graphene on Sapphire by Chemical Vapor Deposition without a Metal Catalyst. *ACS Nano* **2013**, *7*, 385–395.
34. Peng, H.-J.; Hou, T.-Z.; Zhang, Q.; Huang, J.-Q.; Cheng, X.-B.; Guo, M.-Q.; Yuan, Z.; He, L.-Y.; Wei, F. Strongly Coupled Interfaces between a Heterogeneous Carbon Host and a Sulfur-Containing Guest for Highly Stable Lithium-Sulfur Batteries: Mechanistic Insight into Capacity Degradation. *Adv. Mater. Interfaces* **2014**, *1*, 1400227.
35. Huang, J.-Q.; Zhang, Q.; Peng, H.-J.; Liu, X.-Y.; Qian, W.-Z.; Wei, F. Ionic Shield for Polysulfides towards Highly-Stable Lithium-Sulfur Batteries. *Energy Environ. Sci.* **2014**, *7*, 347–353.
36. Chung, S.-H.; Manthiram, A. Bifunctional Separator with a Light-Weight Carbon-Coating for Dynamically and Statically Stable Lithium-Sulfur Batteries. *Adv. Funct. Mater.* **2014**, *24*, 5299–5306.
37. Kim, J.-S.; Hwang, T. H.; Kim, B. G.; Min, J.; Choi, J. W. A Lithium-Sulfur Battery with a High Areal Energy Density. *Adv. Funct. Mater.* **2014**, *24*, 5359–5367.
38. He, G.; Evers, S.; Liang, X.; Cuisinier, M.; Garsuch, A.; Nazar, L. F. Tailoring Porosity in Carbon Nanospheres for Lithium-Sulfur Battery Cathodes. *ACS Nano* **2013**, *7*, 10920–10930.
39. Zhang, B.; Qin, X.; Li, G. R.; Gao, X. P. Enhancement of Long Stability of Sulfur Cathode by Encapsulating Sulfur into Micropores of Carbon Spheres. *Energy Environ. Sci.* **2010**, *3*, 1531–1537.
40. Jayaprakash, N.; Shen, J.; Moganty, S. S.; Corona, A.; Archer, L. A. Porous Hollow Carbon@Sulfur Composites for High-Power Lithium-Sulfur Batteries. *Angew. Chem., Int. Ed.* **2011**, *50*, 5904–5908.
41. Zhang, C. F.; Wu, H. B.; Yuan, C. Z.; Guo, Z. P.; Lou, X. W. Confining Sulfur in Double-Shelled Hollow Carbon Spheres for Lithium-Sulfur Batteries. *Angew. Chem., Int. Ed.* **2012**, *51*, 9592–9595.
42. Bottger-Hiller, F.; Kempe, P.; Cox, G.; Panchenko, A.; Janssen, N.; Petzold, A.; Thurn-Albrecht, T.; Borchardt, L.; Rose, M.; Kaskel, S.; *et al*. Twin Polymerization at Spherical Hard Templates: An Approach to Size-Adjustable Carbon Hollow Spheres with Micro- or Mesoporous Shells. *Angew. Chem., Int. Ed.* **2013**, *52*, 6088–6091.
43. Xin, S.; Yin, Y. X.; Wan, L. J.; Guo, Y. G. Encapsulation of Sulfur in a Hollow Porous Carbon Substrate for Superior Li-S Batteries with Long Lifespan. *Part. Part. Syst. Char.* **2013**, *30*, 321–325.
44. Brun, N.; Sakaushi, K.; Yu, L. H.; Giebeler, L.; Eckert, J.; Titirici, M. M. Hydrothermal Carbon-Based Nanostructured Hollow Spheres as Electrode Materials for High-Power Lithium-Sulfur Batteries. *Phys. Chem. Chem. Phys.* **2013**, *15*, 6080–6087.

45. Xu, G.-L.; Xu, Y.-F.; Fang, J.-C.; Peng, X.-X.; Fu, F.; Huang, L.; Li, J.-T.; Sun, S.-G. Porous Graphitic Carbon Loading Ultra High Sulfur as High-Performance Cathode of Rechargeable Lithium−Sulfur Batteries. *ACS Appl. Mater. Interfaces* **2013**, *5*, 10782–10793.
46. Liu, J.; Yang, T. Y.; Wang, D. W.; Lu, G. Q. M.; Zhao, D. Y.; Qiao, S. Z. A Facile Soft-Template Synthesis of Mesoporous Polymeric and Carbonaceous Nanospheres. *Nat. Commun.* **2013**, *4*, 2798.
47. Li, W. Y.; Zheng, G. Y.; Yang, Y.; Seh, Z. W.; Liu, N.; Cui, Y. High-Performance Hollow Sulfur Nanostructured Battery Cathode through a Scalable, Room Temperature, One-Step, Bottom-up Approach. *Proc. Natl. Acad. Sci. U.S.A.* **2013**, *110*, 7148–7153.
48. Seh, Z. W.; Li, W. Y.; Cha, J. J.; Zheng, G. Y.; Yang, Y.; McDowell, M. T.; Hsu, P. C.; Cui, Y. Sulphur-TiO_2 Yolk-Shell Nanoarchitecture with Internal Void Space for Long-Cycle Lithium-Sulphur Batteries. *Nat. Commun.* **2013**, *4*, 1331.
49. Li, D.; Han, F.; Wang, S.; Cheng, F.; Sun, Q.; Li, W. C. High Sulfur Loading Cathodes Fabricated Using Peapodlike, Large Pore Volume Mesoporous Carbon for Lithium-Sulfur Battery. *ACS Appl. Mater. Interfaces* **2013**, *5*, 2208–2213.
50. Nan, C. Y.; Lin, Z.; Liao, H. G.; Song, M. K.; Li, Y. D.; Cairns, E. J. Durable Carbon-Coated Li_2S Core-Shell Spheres for High Performance Lithium/Sulfur Cells. *J. Am. Chem. Soc.* **2014**, *136*, 4659–4663.